Analytical models to determine in-plane damage initiation and force capacity of masonry walls with openings

Anastasios Drougkas[1*], Rita Esposito[2], Francesco Messali[3], Vasilis Sarhosis[4]

[1] Postdoctoral researcher, Faculty of Civil Engineering and Geosciences, Delft University of Technology, Stevinweg 1, 2628 CN, Delft, The Netherlands (A.Drougkas@tudelft.nl)

[2] Assistant professor, Faculty of Civil Engineering and Geosciences, Delft University of Technology, Stevinweg 1, 2628 CN, Delft, The Netherlands (R.Esposito@tudelft.nl)

[3] Researcher/lecturer, Faculty of Civil Engineering and Geosciences, Delft University of Technology, Stevinweg 1, 2628 CN, Delft, The Netherlands (F.Messali@tudelft.nl)

[4] Associate professor, School of Civil Engineering, University of Leeds, Woodhouse Lane, LS2 9JT, Leeds, United Kingdom (V.Sarhosis@leeds.ac.uk)

Abstract

Masonry panels consisting of piers and spandrels in buildings are vulnerable to in-plane actions caused by seismicity and soil subsidence. Tectonic seismicity can be hazardous for the safety of masonry structures, whereas low-magnitude induced seismicity can be detrimental to their durability due to the accumulation of light damage. This is particularly true in the case of unreinforced masonry. Therefore, the development of models for the accurate prediction of both damage initiation and force capacity for masonry elements and structures is necessary.

In this paper a method based on analytical modelling for the prediction of the damage initiation mode and capacity of stand-alone masonry piers is presented, followed by the expansion of the model through a modular approach to masonry walls with asymmetric openings. The models account for all potential damage and failure modes for in-plane loaded walls.

The stand-alone piers model is applicable to all types of masonry construction. The wall with openings model can be applied as-is to simple buildings but can also be extended to more complex structures with

simple modifications. The model results are compared with numerous experimental cases and exhibit very good accuracy.

Keywords

masonry – earthquake engineering – analytical modelling – limit analysis – in-plane loading

Notation

h	height
h_0	effective height
l	length
t	thickness
m	width of compressive stress fan at centre-height
b	width of compression strut
f_c	compressive strength of masonry
f_t	tensile strength of masonry
f_v	initial shear strength (cohesion)
μ	friction coefficient (tangent of friction angle)
σ	vertical stress
τ	shear stress
V	vertical force
H	horizontal force

Highlights

- Closed-form expressions predict the damage initiation mode and capacity of piers
- Analytical modelling predicts the in-plane shear capacity of masonry walls with openings
- The models are accurate against newly elaborated and existing experimental data

Introduction

State of the art

Masonry structures are vulnerable to seismic loading due to their low tensile and shear strength. While out-of-plane effects can be severely detrimental to the safety of masonry structures, these are often offset when adequate connections allow for the force distribution to the transversal walls via floor diaphragm action. Even if such measures are taken, in-plane failure remains a problem to be dealt with.

Typically, four main failure modes may be clearly distinguished: a) rocking, b) sliding, c) biaxial failure and d) compressive failure. These failure modes, listed in order of appearance under increasing levels of applied vertical stress, define, in combination, a failure envelope for masonry piers under in-plane shear.

Rocking mode failure arises due to the very low tensile strength of masonry perpendicularly to the bed joints, leading to a clear localisation of the bending crack. Models for the rocking capacity can be easily derived through simple equilibrium in bending (Magenes and Calvi, 1997; Roca *et al.*, 2011). Other models have been proposed in design codes (Ministerio delle Infrastrutture e dei Trasporti, 2009). Sliding due to shear, typically localised in bed joints is often described using a Mohr-Coulomb failure criterion. Expressions to determine the capacity in shear at the scale of structural member have been proposed in the literature (Magenes and Calvi, 1997; Tomaževič, 2006) and used in design codes (CEN, 2005). Models for diagonal failure are generally more complex due to the interaction of compression and tension in an area of the pier that is not as clearly defined as in rocking or sliding. Several models for biaxial failure have been proposed in the literature (Turnšek and Cacovic, 1971; Turnšek and Sheppard, 1980; Mann and Muller, 1982), each with different considerations for the dimensions of the pier and the mechanical properties of the masonry composite. The accuracy of biaxial failure models is strongly dependent on the accuracy of the approach used for calculating the tensile strength of masonry, particularly in the horizontal direction. Apart from resorting to computational modelling or simple empirical expressions, there does not appear to be in the literature a demonstrably reliable analytical method for calculating the tensile strength of masonry.

The formulation of models for the prediction of the force capacity of masonry walls with openings is complicated by the frame action made possible by the spandrels, whose failure needs to be accounted for (Beyer, 2012). Simple analytical models accounting for the interaction of failure modes of piers and spandrels in walls with openings are currently lacking in the literature.

The available experimental inventory on masonry stand-alone piers subjected to in-plane shear under vertical stress is extensive (Morandi *et al.*, 2018), and continuously updated (Messali *et al.*, 2020). It includes masonry composites made of different materials, with widely different dimensions and aspect ratios, different boundary conditions and in different bond types. Experimental tests on masonry walls with windows or openings, accompanied by a characterization of the mechanical properties of the masonry composite, are less frequent and feature a smaller variety of boundary conditions (Raijmaker and Vermeltfoort, 1992; Foraboschi, 2009; Parisi, Augenti and Prota, 2014; Drougkas, Roca and Molins, 2019; Korswagen *et al.*, 2019). The relatively small number of experimental tests on walls with openings compared to those performed on single piers has resulted in very limited effort at developing simple models for predicting the force capacity of these assemblages. The abundance of walls with openings in actual practice indicates the potential usefulness of such models for quick capacity checks.

In addition to capacity calculation, the complications introduced by induced seismicity raise the issue of correctly identifying the mode of damage initiation in masonry structures. Combined soil subsidence and low-magnitude seismicity have been shown to impose mostly in-plane demands on masonry structures (Terwel and Schipper, 2018; Van Staalduinen, Terwel and Rots, 2018; Drougkas *et al.*, 2020). These demands are the source of light damage, linked to damage initiation rather than collapse.

Upper-bound approaches for the calculation of the capacity of masonry walls with openings have been proposed in the literature (Vanin and Foraboschi, 2012). Similarly, computational efforts based on finite element (Korswagen *et al.*, 2019; Drougkas *et al.*, 2020) and discrete element analysis (Sarhosis *et al.*, 2019) are relatively abundant. However, a simple model with general applicability for the prediction of the force capacity of masonry walls with openings, one based on the material properties of the masonry composite, is still lacking. Such a model should allow a quick calculation of the capacity of a masonry structure, the prediction of the critical failure mode and the evaluation of the influence of structural intervention on the behaviour without resorting to complex finite element or macro-element modelling.

Furthermore, a simple model for the identification of the in-plane damage initiation mode of masonry piers has not been yet proposed. The need of such a model arises from the increase in low-magnitude induced seismicity near urban centres, which does not necessarily raise the risk of collapse but may be the cause of light damage in masonry structures (Korswagen *et al.*, 2019). A-priori knowledge of the location of damage initiation using simple approaches allows the application of targeted intervention at vulnerable areas. Further, such a model can prove useful as a structural inspection tool, assisting in focusing damage mapping efforts in existing masonry buildings on the areas where damage is expected to arise.

Objectives

The primary objective of the present paper is the presentation of a simple model for the calculation of the in-plane shear capacity of masonry structures. In the context of the paper, the term masonry structure refers to walls with door- or window-openings, in essence masonry portal frames with or without a base spandrel. The model should account for frame action afforded by the spandrel, whose contribution is itself limited by potential damage. Through a modular approach, this model is applicable to masonry elements with multiple openings.

The secondary objective of the paper is the development of a simple model for the prediction of the damage initiation mode in masonry piers subjected to in-plane shear. Essentially, this model should be able to predict the failure mode that arises first in masonry piers under shear. Such a model can be used in stand-alone piers or can be alternatively plugged-in to the proposed model for masonry structures.

The development of the masonry structure model is based on the assembly and evaluation of simple models predicting the capacity of piers in well-defined failure modes. A new model for the biaxial failure of masonry is here proposed which takes into account the effect of the masonry bonding pattern on the tensile strength of masonry in a simple manner. These models are used to define a capacity envelope. The results of the failure models are compared to numerous experimental results from the literature on stand-alone piers.

Moving beyond the application of these models in stand-alone piers, the paper presents a method of application to complex walls with openings, dealing with issues of force distribution and the development of admissible failure modes depending on boundary conditions. This model is validated against case studies from the literature, limiting the investigation to cases where a comprehensive determination of the mechanical properties of the masonry composite is available.

The damage initiation model is developed along the lines of a proposed envelope, similarly to the model for the capacity of piers. A comparison with the corresponding capacity envelope is provided.

Analytical force capacity models for piers

Overview

The dimensions of the pier are $l \times h \times t$ (length × height × thickness). For a given masonry compressive strength f_c and a vertical applied stress σ (negative for compression), the length of the compressed toe b_r, assuming a constant rectangular distribution of vertical stress, or b_t, assuming a triangular distribution, is:

$$
\begin{aligned}
b_r &= -\frac{\sigma}{f_c} l \\
b_t &= -2\frac{\sigma}{f_c} l
\end{aligned}
\tag{1}
$$

For a given set of geometric and material parameters of a stand-alone pier, the applied vertical force V and the horizontal force capacity H are calculated as:

$$
\begin{aligned}
V &= l \cdot t \cdot \sigma \\
H &= l \cdot t \cdot \tau
\end{aligned}
\tag{2}
$$

The shear stress capacity τ is calculated for each of the considered failure modes below. An envelope curve of the capacity can be drawn by varying σ in the range $[0, f_c]$ and considering the minimum value of τ obtained between the considered failure modes. The considered failure modes are illustrated in Figure 1.

The pier is always considered clamped at the base and may be in a cantilever or double-clamped configuration when rotational restraint is provided. The boundary condition at the top determines the effective height h_0 of the pier, with $h_0 = 1.0$ for a cantilever and $h_0 = 0.50$ for a double-clamped configuration.

Rocking mode capacity

In a cantilever configuration, the vertical force V is applied at the centre of the top of the pier, while in a clamped top configuration it is applied at a distance of $b_r/2$ from the edge. The compression strut extends from the point of application of V to the centre of the compressed toe. Through equilibrium of forces and moments, the capacity of a cantilever pier in rocking is:

$$\tau = -\sigma\left(\frac{l}{2} - \frac{b_r}{2}\right)/h \tag{3}$$

while for a clamped top the capacity is:

$$\tau = -\sigma\,(l - b_r)/h \tag{4}$$

In a more general formulation, the horizontal force capacity H can be expressed as the horizontal component of a force acting between two points at a horizontal distance of l and a vertical distance of h whose vertical component is equal to V:

$$H = V\frac{l}{h} \tag{5}$$

Shear mode capacity

For the shear capacity of the pier, the model proposed by Magenes and Calvi is used (Magenes and Calvi, 1997). In the notation of the present paper, the shear capacity is equal to:

$$\tau = \frac{f_v - \mu \cdot \sigma}{1 + h_0/l} \tag{6}$$

where f_v is the initial shear strength (cohesion) and μ is the friction coefficient (tangent of friction angle). As noted in the cited work, these parameters are meant to be understood as globally representing the shear characteristics of the masonry composite rather than that of the bed joints.

Biaxial mode capacity

A new approach based on principal stresses is proposed for calculating the capacity of the pier against biaxial failure. For the interaction of tension and compression, a simple linear failure criterion in planar stress is adopted:

$$f = \frac{\sigma_1}{f_t} - \frac{\sigma_2}{f_c} - 1 \tag{7}$$

where σ_1 is the maximum principal stress (tensile), σ_2 is the minimum principal stress (compressive) and f_t is the tensile strength of the masonry composite. This failure criterion clearly describes the interaction of tensile and compressive stresses in quasi-brittle materials with a shape approximating very closely a linear Mohr-Coulomb criterion.

The compressive stress distribution in a cantilever pier is considered to assume a fan shape, extending along the entire length l of the wall at the top and contracting to the width of the compressive strut b_t at the base. A depiction of this fan shape is illustrated in Figure 2a. The width of the fan m at centre height, where diagonal cracking typically originates, is:

$$m = \frac{l + b_t}{2} \tag{8}$$

In double-clamped piers, the stress fan assumes the shape shown in Figure 2b, with a laterally expanding branch from top to mid-height and a contracting branch from mid-height to base. The angle θ_e of the right external line of the fan with respect to the vertical is limited by the shear strength characteristics of the masonry composite (Roca *et al.*, 2011). Considering that the vertical stress at the edge of the fan is zero, the limit values for the tangent of this angle is:

$$\tan(\theta_e - \theta_c) \leq \mu \tag{9}$$

where θ_c in the angle of the line connecting the centres of the strut edges with respect to the vertical. In this context, the friction coefficient of masonry does not coincide with the friction coefficient of the unit-mortar interface. It is a parameter related to the masonry geometric bond and the resulting interlocking of units, with a minimum value equal to the friction coefficient of the unit-mortar interface. As such, for running bond masonry this coefficient is equal to $\mu = (l_u/2)/(h_u + h_m)$, for Flemish bond it is equal to $\mu = (3\,l_u/4)/(h_u + h_m)$ and for English bond it is $\mu = (l_u/2)/(2h_u + 2h_m)$ with l_u, h_u and h_m being the length of the unit, height of the unit and height of the mortar bed joint respectively. Therefore, the importance of the masonry bonding pattern on both the shear and tensile strength of the masonry becomes apparent. The accuracy of this calculation of the friction coefficient is increased with the increase of the size of the masonry member, due to the clearer formation of diagonal cracks following the masonry bond. The maximum length for m is only limited by the length of the pier.

Based on these conditions, the width m of the fan at centre height of a double-clamped pier is:

$$m = b_t + \min\left[l - b_t, \frac{h}{2}\mu\right] \tag{10}$$

For the orthogonal stress state at the mid-height, it is assumed that the horizontal σ_x stress is zero and that the vertical stress σ_y is evenly distributed. Therefore, it follows that:

$$\begin{aligned} \sigma_x &= 0 \\ \sigma_y &= \sigma \frac{l}{m} \end{aligned} \tag{11}$$

According to Mohr's circle (Beer *et al.*, 2012), the average stress σ_m is:

$$\sigma_m = \frac{\sigma_x + \sigma_y}{2} \tag{12}$$

and, in combination with the adopted failure criterion according to eq. (7), the principal stresses are:

$$\begin{aligned} \sigma_1 &= \frac{2f_t\sigma_m + f_c f_t}{f_t + f_c} \\ \sigma_2 &= \frac{2f_c\sigma_m - f_c f_t}{f_t + f_c} \end{aligned} \tag{13}$$

The radius of Mohr's circle R is:

$$R = \frac{\sigma_1 - \sigma_2}{2} \tag{14}$$

and the resulting shear stress τ_m is:

$$\tau_m = \sqrt{R^2 - {\sigma_m}^2} \tag{15}$$

This shear stress τ_m acts along the length m of the fan at the evaluated position. Therefore, the equivalent stress τ along the length l of the pier is:

$$\tau = \tau_m \frac{m}{l} \tag{16}$$

The determination of the uniaxial horizontal tensile strength of masonry f_t is a complicated issue. It is a function of the tensile strength $f_{t,u}$ of the units, the tensile strength $f_{t,m}$ of the mortar, the tensile strength $f_{t,i}$ of the unit-mortar interface and the shear strength $f_{v,b}$ of the bed joints. Further, it is strongly affected by the masonry bonding pattern, which governs the length at which shear stresses develop. While for masonry in regular bond pattern the vertical tensile strength may be taken as the tensile strength of the unit-mortar interface, the staggered arrangement of the units in, for example, running bond, complicates the failure mechanism. A simple model for the horizontal tensile strength of masonry is therefore introduced. It is based on the identification of three failure modes for the masonry composite in horizontal tension: a) tensile failure of the upper head joint unit-mortar interface together with shearing of the bed joint along the length of half a unit and tensile failure of the lower head joint unit-mortar interface, b) tensile failure of the upper head joint unit-mortar interface together with tensile failure of the bed joint and tensile failure of the lower unit, c) tensile failure of the upper unit together with tensile failure of the bed joint and tensile failure of the lower unit. These modes are illustrated in Figure 3 and are expressed analytically as:

$$\begin{gathered} f_{t,a} = \frac{f_{t,i}\frac{h_u}{2} + f_{v,b} l_o + f_{t,i}\frac{h_u}{2}}{h_u + h_m} \\ f_{t,b} = \frac{f_{t,i}\frac{h_u}{2} + f_{t,m} h_m + f_{t,u}\frac{h_u}{2}}{h_u + h_m} \\ f_{t,c} = \frac{f_{t,u}\frac{h_u}{2} + f_{t,m} h_m + f_{t,u}\frac{h_u}{2}}{h_u + h_m} \\ f_t = min\left[f_{t,a}, f_{t,b}, f_{t,c}\right] \end{gathered} \tag{17}$$

where l_o is the overlap length between the beds of the units which contributes to the shear mechanism. This length can be easily determined for the most common masonry bonds. For running bond it is equal to $l_u/2$, for Flemish and English bond it is equal to $l_u/4$ and in stack bond it is equal to 0. In addition to regular masonry with mortared joints, eq. (17) can account for dry masonry through the contribution of $f_{v,b}$ and for masonry with unfilled head joints by considering $f_{t,i} = 0$.

Compression mode capacity

The capacity of the pier in compression is calculated through a simple superposition of the normal stresses at the base of the pier due to the applied vertical stress σ and the bending moment caused by τ applied at the top of the pier. Limiting the minimum stress to the compressive strength $-f_c$, the shear capacity is equal to:

$$\tau = \frac{(l - b_r)}{6h} f_c \tag{18}$$

Model results and validation

All failure models yield non-negative results for $\sigma \in [0, f_c]$ and produce a capacity envelope as qualitatively shown in Figure 4 for a cantilever pier, defined by the minimum value among the models for a given value of σ. In the case of a clamped pier, the τ envelope is altered only in the region of low vertical stress σ, as both rocking and shear capacity increase. This results in an increase in the range of biaxial failure towards the range of lower vertical stress σ. This shift is critical given that most masonry piers, due to their large dimensions, function at a relatively low level of average vertical stress from self-weight and service loads in buildings.

The results of the model combination are tested against the dataset of experimental results assembled by Morandi et al (Morandi *et al.*, 2018). The dataset includes 188 experimental results of masonry piers subjected to in-plane shear under vertical stress. Material properties are included in the dataset. However, this data is not always fully reported. In the absence of a reported tensile strength f_t this was calculated according to eq. (17). A conservative value of $0.100\ \mathrm{N/mm^2}$ was assumed for $f_{t,i}$ in masonry with mortared head joints, and the tensile strength of the mortar and units was taken as 10% of their respective compressive strengths (Drougkas, Roca and Molins, 2015). Rather than assigning nominal values, the cases where f_v or μ where not reported were disregarded. This filtering resulted in 36 cases with reported f_t and 27 cases with no reported f_t to be considered for analysis, for a total of 63 cases, that is 33% of all reported cases in the cited dataset.

The results of the comparison are plotted in Figure 5. When relying on the reported f_t (Figure 5a) the obtained coefficient of determination R^2 is 0.955 and the mean percentage error MPE is −9.55%, indicating excellent global agreement between the experimental data and analysis results and a tendency of the model to underestimate the capacity. The proposed envelope rarely overestimates the capacity of the piers by more than 15%. The accuracy of the model is noticeably increased when not relying on the reported f_t (Figure 5b) but rather by relying only on the f_t as calculated using eq. (17). The obtained R^2 is slightly increased to 0.962 and the MPE is increased to −5.42%, indicating an enhancement of the model's accuracy, especially in the cases with higher capacity. This improvement validates the accuracy of the proposed model for the tensile strength of masonry and the calculated biaxial failure envelope. Due to the accuracy of the obtained results, the envelope described by these failure models is considered appropriate for application in the analysis of more complex wall structures.

Analytical damage initiation models for piers

Overview

The proposed damage initiation model for stand-alone piers functions similarly to the capacity model. However, instead of calculating the peak shear force for a specific failure type, it calculates the shear force activating a specific failure type. It may, therefore, be used for identifying the sequence of damage mode initiation and propagation in stand-alone piers loaded in-plane.

Under the assumption that the pier is uncracked before damage initiation, the normal stresses can be easily computed through superposition of the stresses due to σ and τ applied at the top of the pier. Similarly, the distribution of shear stress along the length of the pier assumes a parabolic shape, with the maximum shear stress being 1.5 times the average (Timoshenko, 1940).

Rocking mode initiation

Damage initiation in rocking occurs under the following conditions: a) a constant vertical stress distribution at the top and a triangular vertical stress distribution at the base are assumed, b) for the maximum stress at the least compressed toe: $\sigma_{\max} = f_{t,i}$, c) for the minimum stress at the compressed toe: $\sigma_{\min} \geq -f_c$.

According to moment and force equilibrium, and based on the above conditions, the resulting value for the minimum stress is:

$$\sigma_{\min} = 2\sigma - f_{t,i} \tag{19}$$

while the damage initiation shear stress is:

$$\tau = \left(f_{t,i} - \sigma\right)\frac{l}{6h} \tag{20}$$

Shear mode initiation

The conditions for shear mode initiation are: a) a trapezoidal vertical stress distribution is assumed at the base, b) for the maximum stress at the least compressed toe: $\sigma_{\max} \leq f_{t,i}$, c) for the minimum stress at the compressed toe: $\sigma_{\min} \geq -f_c$, d) the maximum shear stress due to the trapezoidal distribution needs to reach the shear strength. Therefore, $\tau = (f_v - \mu \cdot \sigma_{\max})/1.5$.

Based on these assumptions and applying moment equilibrium, the values for the minimum and maximum stress are:

$$\sigma_{\max} = \frac{f_v \cdot h - (2 \cdot \mu \cdot h + l)\sigma}{h \cdot \mu + l} \tag{21}$$

$$\sigma_{\min} = -\frac{l \cdot \sigma + 4 \cdot f_v \cdot h}{4 \cdot h \cdot \mu + l}$$

while the value for the damage initiation shear stress is:

$$\tau = 2\frac{f_v - \sigma \cdot \mu}{12 \cdot h \cdot \mu + 3 \cdot l}l \tag{22}$$

Biaxial mode initiation

The biaxial mode initiation stress is calculated similarly to the capacity according to eq. (8) through eq. (16). Due to the assumption that no other damage initiation mode has arisen, the pier remains uncracked and the stress fan is vertical, the horizontal force being resisted by friction. Therefore, the width of the fan m is equal to the length of the pier l. Due to the parabolic shear stress distribution along the length of the pier, the damage initiation shear stress is equal to:

$$\tau = \frac{\tau_m}{1.5} \tag{23}$$

Model results and validation

The three mode initiation models can be combined to produce a damage initiation envelope. This envelope is additionally delimited by the compressive failure model as defined in eq. (18). The brittleness of the compressive failure mode results in the coincidence of damage initiation and force capacity. Plotting the damage initiation envelope for a masonry pier results in a typical curve shown in Figure 6, where a comparison with the capacity envelope is shown. The damage initiation envelope is always below the capacity envelope.

The range of normalised vertical stresses for which damage initiates through pure rocking is greater than the range where rocking determines the capacity. This is true for the shear mode as well. Conversely, the range of biaxial mode initiation is limited compared to the capacity envelope. Due to the usually low level of global vertical stress under which masonry piers typically operate in buildings (Heyman, 1966), it is expected that the majority of piers will feature rocking or shearing damage initiation, followed by rocking, shearing or, less commonly, biaxial failure.

The damage initiation model is validated against a series of experiments carried out on piers at Delft University of Technology (Esposito and Ravenshorst, 2017; Korswagen *et al.*, 2017), coupled with extensive material characterisation (Jafari and Esposito, 2016, 2017). The geometric and material parameters are reported in Table 1. The experiments include two different sets of materials, different masonry bonds, different boundary conditions and varying vertical pre-compression levels.

The damage initiation and final failure mode was reported in three of the cases (TUD_COMP_20, TUD_COMP_21, TUD_COMP_22), while for one of the cases (TUD_COMP_47/48) the crack pattern was objectively registered using digital image correlation (DIC). Systematic documentation and objective interpretation of damage initiation in experimental reports is often problematic without the use of DIC or other optical methods for crack tracking. Damage initiation is typically reported in terms of visible diagonal cracking, which cannot arise without prior initiation of some degree of rocking damage. Localised toe crushing may also be reported, but this phenomenon is associated with practically all damage initiation and capacity models and is, therefore, not indicative of the overall failure mode by itself. Nevertheless, even damage reported in simple terms can assist in interpreting damage initiation modes in masonry piers.

Overall, the model exhibits very good accuracy in both capacity calculation and in predicting the damage initiation and failure mode. In cases TUD_COMP_21, TUD_COMP_22 and TUD_COMP_47/48 the model was able to predict the shift from a damage initiation mode based on rocking/sliding to a failure mode based on diagonal cracking. The number of suitable experimental cases suitable for validation of the proposed model, which need to include comprehensive material characterisation and unambiguous reporting of the damage initiation force and mode, is currently small, especially compared to the number of cases suitable for validation of the capacity model. Further experimental investigation focusing on damage initiation is thus motivated.

Strut & fan model for walls with openings

General model description

In the context of the proposed approach, modelling of masonry walls with openings under in-plane loads requires: 1) the discretisation of the frame into individual components, 2) the distribution of forces and stresses in these components, 3) the identification of potential failure modes according to the arrangement of the components and the boundary conditions.

The discretisation of a masonry wall with a single opening is shown in Figure 7, along with the notation used hereafter for dimensions and loads. The wall consists of 8 components arranged in a regular 3×3 grid. Three components for the spandrel (S_1, S_2 and S_3), two components for the piers (P_1 and P_3) and three components for the base (B_1, B_2 and B_3) are considered. The piers can have different lengths, thus allowing the analysis of asymmetric structures. Each component can be assigned its own thickness t and set of material properties. Additionally, the vertical load at the top of each pier and of the spandrel can be different. A height of $h_1 = 0$ reduces the model to a portal frame, while all the other dimensions can only be greater than 0. The horizontal loading direction is towards the positive of the x axis. Vertical compression is applied towards the negative of the y axis.

In the modular approach proposed, the wall W is composed of a pair of sub-systems: L (left) and R (right), connected with a central spandrel. Each sub-system consists of a single base, pier and spandrel. The capacity of the wall is dependent on the capacity of the individual sub-systems and the effect of their interaction through spandrel action.

Boundary conditions and spandrel function

As in the case of stand-alone piers, the wall is considered clamped at the base. For the boundary condition at the top, the wall may be in a) cantilever, b) clamped or c) clamped with vertical translational restraint configuration.

The boundary conditions and construction details at the top of the wall affect the function of the spandrel in providing frame action. In particular, for a cantilever configuration, two cases are distinguished: a) a “weak” connection with the piers, due to the absence of structural elements above the spandrel, and b) a “strong” connection with the piers, provided by steel or reinforced concrete capping beams or a strong lintel. In the former, the S_2 spandrel component responds to horizontal loading by “rocking” between the two piers: a hinge is formed at the top right corner of S_1 and another at the left bottom corner of S_3. In the latter case, the spandrel elements respond jointly. For the clamped and clamped with vertical restraint configurations, it is always considered that the spandrel provides a “strong” connection. The two types of spandrel function are illustrated in Figure 8.

The combined effect of boundary conditions, spandrel action and assumption on load transfer from the top to the spandrel blocks during flexure (Beyer, 2012) control the static determinacy of the wall system, which may be treated as a portal frame with internal hinges. The “weak” spandrel provides two internal hinges, while the "strong" spandrel provides one. Therefore, the static indeterminacy of the wall in the first case is 1 while for the second case it is 2. The added rotational restraint from a double-clamped condition adds an additional degree of indeterminacy.

Modelling assumptions

The stress distribution in the components is represented through a system of compressive struts and fans. The compressive struts develop between two formed plastic hinges. Fans develop between two continuous lines of applied vertical displacement or between one such line and a plastic hinge.

Concerning the distribution of the compressive stresses, it is assumed that the vertical stress σ_1 is distributed to pier P_1, while both vertical stresses σ_2 and σ_3 are borne by pier P_3, due to the loading direction (Roca, 2006). The transfer of vertical load from the spandrel S_2 above the opening constitutes the frame action of the wall.

Plastic hinges are formed due to yielding in compression and have a width of b calculated as per the pier model through eq. (1).

Sub-system failure shapes

Eight arrangements of plastic hinges are possible for a sub-system, illustrated in Figure 9. Stress fans are depicted in light blue, with the direction of the stress flow indicated by arrows. Compressive struts are indicated in deeper blue colour. The expansion of the stress fan between hinges as expressed in eq. (10) and illustrated in Figure 2 is not shown for clarity of the illustrations. The plastic hinges are formed at the edges of the struts or at the convergence locus between a laterally contracting and an expanding stress fan. The locations of the plastic hinges coincide with the points of contact between blocks, i.e. the points where the piers meet the base or the spandrel, where stresses due to in-plane shear tend to concentrate. The resulting mechanisms are representative of those found in experimental practice and used to interpret the failure mode of walls with openings (Vanin and Foraboschi, 2012).

The disposition of the struts and fans determines where the failure checks are performed. This point is illustrated by commenting on the difference between shapes 1, 2 and 3. In shape 1, the spandrel, pier and base are checked individually. In shape 2 all three components are checked as one. In shape 3 the base is checked individually while the spandrel and pier are checked as one component.

Individual failure checks are executed according to the model for stand-alone piers: a) all components are checked against biaxial failure according to eq. (16), b) all components are checked in compression according to eq. (18), c) piers are checked in shear according to eq. (6), c) rocking failure is checked according to eq. (5) by calculating the horizontal force component between plastic hinges or, in the absence of a second plastic hinge, by assuming a resultant force at the centre of a fan extending towards the direction of loading (positive x direction).

The failure checks in sub-system L are straightforward due to the sub-system only bearing the vertical and horizontal forces applied on S_1. Sub-system B bears the vertical and horizontal forces applied on both S_2 and S_3. For a "weak" spandrel, V_2 is transferred to the lower right corner of S_3, while for a "strong" spandrel it is applied at the centre of S_2, providing an increased lever-arm and increased rocking capacity. In the case of a "strong" spandrel, an additional biaxial strength check is performed for S_2, considering a stress fan from the top of S_2 to the top of P_2, where it assumes a width as defined in Figure 9.

Based on these calculations, the capacity $\tau_{A,i}$ and $\tau_{B,i}$ of each sub-system L or R for the failure shapes $i \in [1,8]$ is calculated.

Combination of sub-system failure shapes

The sub-system failure shapes are combined in pairs. Each pair defines a potential failure mode and total capacity for the wall. These capacity sums can be expressed as:

$$\boldsymbol{C}(i,j) = \left(\tau_{L,i} + \tau_{R,j}\right), \quad i,j \in [1,8] \tag{24}$$

The capacity of the wall τ_W is defined as the minimum element in $\boldsymbol{C}$. However, due to their interaction in the wall and due to boundary conditions, not all sub-system failure shapes are allowed in the complete wall structure. The boundary conditions and geometry of the wall affect the stress distribution and potential failure modes as follows: a) cantilever walls with "weak" spandrels require the formation of 2 hinges, b) cantilever walls with "strong" spandrels require 3 hinges, c) hinges cannot form at the top of cantilever walls with "strong" spandrels for maintaining continuity of the applied vertical stress, d) double-clamped walls require 4 hinges, e) double-clamped walls with vertical restraint require 4 hinges, but the bending failure mode is inactivated, f) the central part B_2 of the base restricts the rotation of components B_1 and B_3 (Caliò, Marletta and Pantò, 2012), therefore, no plastic hinge can form at the base of B_1 or B_3, unless a sufficient gap is provided between the base components.

Based on the above conditions, and assuming that no gaps are provided between the base components, the allowable failure shape combinations are: a) $\boldsymbol{C}(3,3)$, $\boldsymbol{C}(3,7)$, $\boldsymbol{C}(3,8)$, $\boldsymbol{C}(7,3)$, $\boldsymbol{C}(7,7)$, $\boldsymbol{C}(7,8)$, $\boldsymbol{C}(8,7)$, and $\boldsymbol{C}(8,8)$ for a cantilever wall with a "weak" spandrel, b) $\boldsymbol{C}(1,3)$, $\boldsymbol{C}(3,1)$, $\boldsymbol{C}(1,7)$ and $\boldsymbol{C}(7,1)$ for a cantilever wall with a "strong" spandrel, c) $\boldsymbol{C}(1,1)$, $\boldsymbol{C}(1,6)$ and $\boldsymbol{C}(6,1)$ for the double-clamped, with or without vertical restraint.

Model results and validation

The proposed model for the masonry wall capacity is validated against experimental cases from the literature (Raijmaker and Vermeltfoort, 1992; Foraboschi, 2009; Lobato Paz, 2009; Vanin and Foraboschi, 2012; Parisi, Augenti and Prota, 2014; Esposito and Ravenshorst, 2017; Korswagen *et al.*, 2017). Among the findings in the literature, the list of cases used was confined to those in which material parameters were reported. It includes both walls with window openings and portal frames, i.e. where $h_1 = 0$. Due to the small number of such available campaigns, nominal shear characteristics were assumed where they were missing in order to not overly limit the application cases (Van der Pluijm, 1992). The tensile strength as calculated according to eq. (17) and the friction angle of the masonry as calculated in subsection 0 are also reported. Concerning boundary conditions, walls were tested in cantilever with "strong" spandrel ('C') and double-clamped with vertical restraint ('V') configuration. The vertical load was only applied on the piers in a few instances. All parameters used and results obtained are presented in Table 2

The case studies involve different types of loading regimes. Three cases involve monotonic loading (Raijmaker and Vermeltfoort, 1992; Lobato Paz, 2009; Parisi, Augenti and Prota, 2014), three cases involve loading-unloading cycles in one direction (Foraboschi, 2009; Vanin and Foraboschi, 2012; Korswagen *et al.*, 2017) and one case involves cyclic loading in two directions (Esposito and Ravenshorst, 2017). Since the proposed model does not account for degradation due to repeated or cyclic loading, the modelling approach is not altered to accommodate this fact. Simulation of cyclic response in the context of this model would involve the degradation of the shear strength in the bed joints, the opening of the head joints in tension, which would reduce the horizontal tensile strength of masonry, and the adjustment of the strut disposition due to diagonal cracking.

The difference in wall capacity due to uneven piers, accompanied by a shift in failure mode, is captured in the simulation of the experiments by Esposito & Ravenshorst (Esposito and Ravenshorst, 2017). The quarter-scale experiments by Lobato (Lobato Paz, 2009) and full-scale experiments by Foraboschi & Vanin (Foraboschi, 2009; Vanin and Foraboschi, 2012) illustrate the shift in capacity due to an increasing vertical load, an increase indicative of the global friction angle of the masonry. The accuracy of the model in simulating large piers connected by a spandrel, namely portal frames without the base, is shown in the simulation of the experiments by Parisi et al (Parisi, Augenti and Prota, 2014). Finally, the model captures the significant effect of boundary conditions on the response, as illustrated in the high capacity obtained in the experiments by Raijmaker, which was vertically restrained, resulting in a force capacity nearly double that of a double-clamped model (Raijmaker and Vermeltfoort, 1992).

Overall, the model exhibits good accuracy, with no marked tendency to under- or overestimate the force capacity. A slight divergence from the linear trend obtained in the experiments by Lobato is obtained, pointing towards a possible discrepancy between the actual friction angle of masonry and the value obtained in the model. The capacity obtained by Parisi et al is well approximated, potentially due to the simple failure mode registered in the piers. The differences between the analysis results and the experimental results in the related experimental cases by Foraboschi and Vanin & Foraboschi are not easy to explain. Despite the repeated nature of the loading in the experiments, the model underestimates the force capacity nearly throughout. It is possible that this systematic error is due to the unit-mortar interface tensile strength or shear strength being higher than assumed. This is also potentially true in the experiments by Korswagen and Esposito & Ravenshorst. The large overestimation obtained in one of the experiments by Foraboschi (under 0.09 N/mm^2 vertical stress), due to the very low level of applied vertical stress, can only be accounted for in the model by a change in the spandrel action. A "weak" spandrel assumption results in a calculated peak force of 11.7 kN versus the experimental value of 18.2 kN. It is possible, therefore, that the actual conditions during the experiment were an intermediate between a "strong" and a "weak" spandrel.

A comparison of the experimentally obtained failure modes, where these were reported, with the numerically calculated results is presented in Table 3. Overall, there is very good agreement between the experimental and numerical results, especially regarding the prediction of the failure mode of the left sub-system. This sub-system appears to be susceptible to bending failure due to the lower overall vertical load borne by it, validating the assumption of the transfer of vertical load to the right sub-system by the spandrel. Regarding the failure of the right sub-system, the model is able to predict the failure mode for nearly all cases. Reports on the experimental results through photos and text descriptions reveal a more mixed failure mode, with cracking being shown in both the spandrel and the bases, such as in the experiments by Vanin & Foraboschi. In this sense the model is capable of predicting the failure mode at least in part. Finally, regarding the discrepancy in the prediction for the Esposito and Ravenshorst case, where the sub-system failed at the base, with the spandrel failing in subsequent loading cycles, the model predicts a capacity of the spandrel roughly 1 kN or 6% higher than for the base. The discrepancy is therefore considered minor as a very slight change in material properties would produce the recorded failure type.

Sensitivity study

The influence of a number of geometric and material parameters on the predicted force capacity is investigated through a sensitivity study. The Esposito & Ravenshorst case study is elected for this task due to the extensive material characterisation campaign that accompanies it. The parameters include the compressive strength of masonry f_c, the tensile strength of the unit-mortar interface $f_{t,i}$ and the initial shear strength of the unit-mortar interface f_v. Additionally, the influence of the length of units l_u, the height of units h_u and the thickness of the mortar joints t_m is similarly investigated. The results are presented in Figure 10. For ease of presentation in a single graph, the parameters have been normalised by division with their reference values as listed in Table 2. The normalised parameters are presented using a hat operator, meaning that the normalised compressive strength of masonry is shown as $\hat{f}_c$ and the force capacity is shown as $\widehat{H}_{mod}$.

The force capacity is not particularly sensitive to the compressive strength of masonry $\hat{f}_c$. This is consistent with the rocking of the piers being governed primarily by the geometry of the structure. Conversely, the tensile strength of the unit-mortar interface $\hat{f}_{t,i}$ plays a more important role, being directly involved in the calculation of the tensile strength of the masonry. Similarly, the shear strength $\hat{f}_v$ exerts the greatest influence on the peak force due to it being involved in both the horizontal tensile strength and shear strength of the masonry.

The geometric properties of the units and mortar appear to play a very significant role in the force capacity. Firstly, it is found that increasing the length of units $\hat{l}_u$ increases the force capacity due to an increase in the horizontal tensile strength of masonry. Secondly, the thickness of the mortar joints $\hat{t}_m$ does not strongly affect the force capacity, although it is noted that an increase in the mortar joint in reality would lead to a slight decrease in the compressive strength of masonry. Finally, increasing the height of the units $\hat{h}_u$ leads to a reduction of the force capacity due to a decrease in the horizontal tensile strength of masonry.

In addition to the study of numerical parameters, the bonding pattern and boundary conditions are included in the study. These results are presented in Table 4, the reference case being the one with an English bond pattern and a cantilever with "strong" spandrel boundary condition.

While the stack bond results in a marginal reduction of the calculated force capacity, switching to a Flemish or running bond leads to a roughly 23% increase. In all three cases (stack, Flemish, running bond) the failure of the wall was due to bending of the left sub-system and biaxial failure of the spandrel in the right sub-system. In the first case the change in tensile strength of masonry was not enough for making a substantial change in the result. However, in the latter two cases, the increase in the tensile strength was enough to make a difference in the capacity of the spandrel. The boundary conditions, as expected, have a strong effect on the calculated force capacity. Double clamped and vertically restrained conditions result in an increase of 14.3% and 45.5% of the force capacity respectively. Conversely, the “weak” spandrel cantilever results in a 15.4% decrease in the force capacity, illustrating the effect of a rigid top beam or lintel.

The sensitivity study illustrates the delicate interaction of all parameters involved in the prediction of the in-plane shear force capacity of masonry walls. The dimensions of the units, the bonding pattern, boundary conditions and properties of the unit-mortar interface all play a significant role in the load bearing mechanism and should, therefore, always be the subject of careful investigation.

Conclusions

An analytical model for the prediction of the in-plane capacity of masonry piers and walls with openings is presented. The model considers all major geometric and material parameters, including the bond type, for the calculation of the capacity. Additionally, an analytical model is proposed for the prediction of the damage initiation mode in masonry piers under in-plane shear. Apart from geometric and material properties, no further numerical parameters or major empirical assumptions are needed for analysis.

The model accounts for all potential failure modes normally encountered in masonry walls subjected to a combination of in-plane vertical and horizontal loading. Unequal vertical loading, asymmetric piers and local variations in material properties can be easily introduced in the analysis.

The basis of the model is validated against numerous standalone pier experimental tests, while the model for walls with openings is similarly validated against several case studies with different material properties, dimensions, bonding patterns and boundary conditions.

The model provides a very efficient and accurate method for the capacity assessment of simple structures subjected to in-plane shear loading under vertical stress. The damage initiation model provides a simple means of highlighting weaknesses in masonry piers, thus allowing efficient intervention design for the strengthening of masonry structures against damage initiation. The advantages of the model include the calculation of the damage initiation and capacity forces with simple analytical expressions and no computational resources nor reliance on empirical simplifications. This facilitates the quick completion of sensitivity studies, which, given the large number of material and geometric parameters involved in the problem, have been demonstrated to be crucial in understanding the behaviour of masonry walls with openings. Further, the resulting failure mechanisms can be unambiguously evaluated by the user, whether the model is used for research or in engineering practice. Disadvantages of the model include the lack of capabilities for generating force-displacement data, a reliance on numerous material parameters and an inability to account for cyclic loading or load reversal. It is noted that the first disadvantage is shared with all methods based on limit-analysis, the second is shared with most other computational approaches currently available and the third can be addressed in a future effort involving more detailed constitutive modelling.

The proposed model presents opportunities for future work pertaining to the simulation of structural reinforcement, such as in the form of embedded bars. The contribution of horizontal bars can be introduced in the tensile strength for the biaxial failure check. Vertical bars can increase the rocking mode capacity when anchored at the base of cantilever walls, or at the base and top of double-clamped piers. Finally, diagonal bars can restore or increase the cohesion in damaged zones.

Data availability statement

All data, models, or code that support the findings of this study are available from the corresponding author upon reasonable request.

References

Beer, F. P. *et al.* (2012) *Mechanics of Materials*. New York: McGraw-Hill Professional.

Beyer, K. (2012) 'Peak and residual strengths of brick masonry spandrels', *Engineering Structures*. Elsevier Ltd, 41, pp. 533–547. doi: 10.1016/j.engstruct.2012.03.015.

Caliò, I., Marletta, M. and Pantò, B. (2012) 'A new discrete element model for the evaluation of the seismic behaviour of unreinforced masonry buildings', *Engineering Structures*, 40, pp. 327–338. doi: 10.1016/j.engstruct.2012.02.039.

CEN (2005) *EN 1996-1-1 — Eurocode 6 - Design of masonry structures - Part 1-1: General rules for* *reinforced and unreinforced masonry structures*.

Drougkas, A. *et al.* (2020) 'In-plane seismic behaviour of retrofitted masonry walls subjected to subsidence-induced damage', *Engineering Structures*. Elsevier, 223(July), p. 111192. doi: 10.1016/j.engstruct.2020.111192.

Drougkas, A., Roca, P. and Molins, C. (2015) 'Numerical prediction of the behavior, strength and elasticity of masonry in compression', *Engineering Structures*, 90, pp. 15–28. doi: 10.1016/j.engstruct.2015.02.011.

Drougkas, A., Roca, P. and Molins, C. (2019) 'Experimental Analysis and Detailed Micro-Modeling of Masonry Walls Subjected to In-Plane Shear', *Engineering Failure Analysis*, 95, pp. 82–95. doi: 10.1016/j.engfailanal.2018.08.030.

Esposito, R. and Ravenshorst, G. . J. P. (2017) *Quasi-static cyclic in-plane tests on masonry components 2016/2017. Report number: C31B67WP3-4*, *Report number C31B67WP3-4*. TU Delft.

Foraboschi, P. (2009) 'Coupling effect between masonry spandrels and piers', *Materials and Structures*, 42(3), pp. 279–300. doi: 10.1617/s11527-008-9405-7.

Heyman, J. (1966) 'The stone skeleton', *International Journal of Solids and Structures*, 2(2), pp. 249–279. doi: 10.1016/0020-7683(66)90018-7.

Jafari, S. and Esposito, R. (2016) *Material tests for the characterisation of replicated solid calcium silicate brick masonry. Report number: C31B67WP1-9*, *Report number: C31B67WP1-9*. TU Delft.

Jafari, S. and Esposito, R. (2017) *Material tests for the characterisation of replicated solid clay brick masonry. Report number: C31B67WP1-12*, *Report number: C31B67WP1-12*. TU Delft.

Korswagen, P. A. *et al.* (2017) *Damage sensitivity of Groningen masonry structures - Experimental and computational studies. Report number: C31B69WP0-11*, *Report number C31B69WP0-11*. TU Delft.

Korswagen, P. A. *et al.* (2019) 'Crack initiation and propagation in unreinforced masonry specimens subjected to repeated in-plane loading during light damage', *Bulletin of Earthquake Engineering*. Springer Netherlands, 17(8), pp. 4651–4687. doi: 10.1007/s10518-018-00553-5.

Lobato Paz, E. M. (2009) *Método simple para el análisis de muros de obra de fábrica con aberturas bajo solicitaciones en su plano*. PhD dissertation.

Magenes, G. and Calvi, G. M. (1997) ‘In-plane seismic response of brick masonry walls’, *Earthquake Engineering and Structural Dynamics*, 26(11), pp. 1091–1112. doi: 10.1002/(SICI)1096-9845(199711)26:11<1091::AID-EQE693>3.0.CO;2-6.

Mann, W. and Muller, H. (1982) ‘Failure of Shear-Stressed Masonry. An Enlarged Theory, Tests and Application to Shear Walls’, in *Proceedings of British Ceramic Society*, pp. 223–235.

Messali, F. *et al.* (2020) *Experimental investigation of the in-plane cyclic behaviour of calcium silicate brick masonry walls*, *Bulletin of Earthquake Engineering*. Springer Netherlands. doi: 10.1007/s10518-020-00835-x.

Ministerio delle Infrastrutture e dei Trasporti (2009) *Circolare 2 febbraio 2009, n. 617 Istruzioni per l’applicazione delle ‘Nuove norme tecniche per le costruzioni’ di cui al decreto ministeriale 14 gennaio 2008*.

Morandi, P. *et al.* (2018) ‘Development of a dataset on the in-plane experimental response of URM piers with bricks and blocks’, *Construction and Building Materials*. Elsevier Ltd, 190, pp. 593–611. doi: 10.1016/j.conbuildmat.2018.09.070.

Parisi, F., Augenti, N. and Prota, A. (2014) ‘Implications of the spandrel type on the lateral behavior of unreinforced masonry walls’, *Earthquake Engineering & Structural Dynamics*, 43(11), pp. 1867–1887. doi: 10.1002/eqe.2441.

Van der Pluijm, R. (1992) ‘Material properties of masonry and its components under tension and shear’, in *6th Canadian Masonry Symposium, Saskatoon*, pp. 675–686.

Raijmaker, T. M. . and Vermeltfoort, A. T. (1992) *Deformation controlled meso shear tests on masonry piers. Rep. B-92-1156, TNO- BOUW/TU Eindhoven*, *Rep. B-92-1156, TNO- BOUWITU Eindhoven*. TNO-BOUW/TU Eindhoven.

Roca, P. (2006) ‘Assessment of masonry shear-walls by simple equilibrium models’, *Construction and Building Materials*, 20(4), pp. 229–238. doi: 10.1016/j.conbuildmat.2005.08.023.

Roca, P. *et al.* (2011) 'Capacity of shear walls by simple equilibrium models', *International Journal of Architectural Heritage*, 5(4–5), pp. 412–435. doi: 10.1080/15583058.2010.501481.

Sarhosis, V. *et al.* (2019) 'Evaluation of modelling strategies for estimating cumulative damage on Groningen masonry buildings due to recursive induced earthquakes', *Bulletin of Earthquake Engineering*, 17(8), pp. 4689–4710. doi: 10.1007/s10518-018-00549-1.

Van Staalduinen, P., Terwel, K. and Rots, J. G. (2018) *Onderzoek naar de oorzaken van bouwkundige schade in Groningen Methodologie en case studies ter duiding van de oorzaken. Report number: CM-2018-01*, *Report number: CM-2018-01*. TU Delft.

Terwel, K. and Schipper, R. (2018) 'Innovative ways of dealing with existing problems: How to reliably assess the cause of damage of masonry structures in an area with man-induced earthquakes?', in *IABSE Symposium, Nantes 2018: Tomorrow's Megastructures*, pp. S23-39-S23-46. Available at: https://www.scopus.com/inward/record.uri?eid=2-s2.0-85059364074&partnerID=40&md5=4a8d359c7cd1dcfccb4bdfa142c2c747.

Timoshenko, S. (1940) *Strength Of Materials*. D. Van Nostrand Company.

Tomaževič, M. (2006) *Earthquake-Resistant Design of Masonry Buildings*, *Innovation in Structures and Construction - Vol. 1*. London: Imperial College Press.

Turnšek, V. and Cacovic, F. (1971) 'Some experimental results on the strength of brick masonry walls', in *Proceedings of the 2nd Intern. Brick Masonry Conference*, pp. 149–156.

Turnšek, V. and Sheppard, P. (1980) 'The shear and flexural resistance of masonry walls', in *International Research Conference on Earthquake Engineering*.

Vanin, A. and Foraboschi, P. (2012) 'In-plane behavior of perforated brick masonry walls', *Materials and Structures*, 45(7), pp. 1019–1034. doi: 10.1617/s11527-011-9814-x.

List of Tables

List of Figures

Figure 9 Potential failure shapes for base-pier-spandrel sub-system. Disposition of stress fans and compressive struts.

Figure 10 Sensitivity study: effect of a) material properties and b) geometric parameters on force capacity.

Table 1 Experimental case studies for pier model validation: geometric and material parameters. Force capacity prediction error in parentheses.

Parameter	Symbol	Unit	Case study			
Specimen name	-	-	TUD_COMP_20	TUD_COMP_21	TUD_COMP_22	TUD_COMP_47/48
Reference	-	-	(Esposito and Ravenshorst, 2017)	(Esposito and Ravenshorst, 2017)	(Esposito and Ravenshorst, 2017)	(Esposito and Ravenshorst, 2017)
Pier length	l	mm	1100	3070	3070	3070
Pier height	h	mm	2778	2710	2710	2710
Pier thickness	t	mm	102	100	210	100
Unit length	l_u	mm	214	210	210	210
Unit height	h_u	mm	72	50	50	50
Mortar bed joint height	h_m	mm	10	10	10	10
Unit compressive strength	f_{cu}	N/mm^2	13.26	28.30	28.30	28.30
Mortar compressive strength	f_{cm}	N/mm^2	7.57	3.81	3.81	3.81
Masonry compressive strength	f_c	N/mm^2	6.35	14.02	10.67	11.35
Unit-mortar interface tensile strength	f_{ti}	N/mm^2	0.12	0.15	0.15	0.09
Initial shear strength	f_v	N/mm^2	0.13	0.12	0.12	0.14
Masonry bond	-	-	Running	Running	English	Running
Vertical stress	$-\sigma$	N/mm^2	0.63	0.36	0.36	0.46
Boundary condition	-	-	Cantilever	Double-clamped	Cantilever	Cantilever
Damage initiation - experimental	-	-	Rocking	Shear/rocking	Rocking	Rocking
Failure mode – experimental	-	-	Rocking	Biaxial	Rocking	Biaxial
Shear force capacity – experimental	H_{exp}	kN	15.1	98.1	117.2	112.5
Damage initiation – model	-	-	Rocking	Rocking	Rocking	Rocking
Failure mode – model	-	-	Rocking	Biaxial	Rocking	Biaxial
Shear force capacity – model	H_{mod}	kN	13.5 (-10.6%)	100.6 (2.5%)	120.2 (2.6%)	106.2 (-5.6%)

Table 2 Comparison of wall with opening capacity model with experimental results from the literature. Predicted force error in parentheses.

Ref.	h_1	h_2	h_3	l_1	l_2	l_3	t	f_c	f_v	μ	f_t	$-\sigma$	Boundary conditions	Masonry bond	H^+_{exp}	H^+_{mod}	H^-_{exp}	H^-_{mod}
–	mm	mm	mm	mm	mm	mm	mm	N/mm²	N/mm²	–	N/mm²	N/mm²	–	–	kN	kN	kN	kN
(Lobato Paz, 2009)	90	90	90	150	75	112.5	35	18.9	0.46	2.42	1.70	0.645	C	Running	4.9	5.7 (16.3%)	-	-
												1.132			7.7	9.6 (24.7%)	-	-
												1.858			13.1	12.5 (-4.6%)	-	-
												2.540			13.2	14.5 (9.8%)	-	-
												3.236			15.9	16.3 (2.5%)	-	-
												4.036			17.7	17.9 (1.1%)	-	-
(Parisi, Augenti and Prota, 2014)	0	2300	1000	1700	1700	1700	310	3.73	0.15	1.36	0.26	0.373[b]	C	Running	184	171.5 (-6.8%)	-	-
(Vanin and Foraboschi, 2012)	325	1170	845	930	880	930	240	1.21	0.15[a]	2.36	0.16	0.300[b]	C	Flemish	63	51.7 (-17.9%)	-	-
												0.179[b]			48	37.8 (-21.3%)	-	-
												0.090[b]			18	19.4 (7.7%)	-	-
(Foraboschi, 2009)	380	1210	1180	1025	1070	1025	250	1.21	0.15[a]	2.64	0.16	0.270[b]	C	Flemish	64.2	60.4 (-5.9%)	-	-
												0.179[b]			59.8	43.2 (-27.8%)	-	-
												0.090[b]			18.2	24.4 (34.1%)	-	-
(Korswagen et al., 2017)	530	1510	650	870	780	1420	100	11.35	0.13	1.75	0.37	0.120	C	Running	22.2	19.3 (-13.1%)	-	-
(Esposito and Ravenshorst, 2017)	540	1680	490	870	1000	1200	210	10.67	0.2	0.88	0.32	0.340	C	English	85.4	84.2 (-1.4%)	94.1	90.4 (-3.9%)
(Raijmaker and Vermeltfoort, 1992)	350	350	350	430	210	325	100	10.5	0.35	1.75	0.66	0.300	V	Running	41.5	45.6 (9.9%)	-	-

[a] assumed value

[b] vertical load applied over pillars only

Table 3 Comparison of experimentally obtained and numerically derived failure modes for walls with openings.

Reference	$-\sigma$ N/mm^2	Load direction	Experimental results		Numerical results	
			Left sub-system	Right sub-system	Left sub-system	Right sub-system
(Lobato Paz, 2009)	0.645	+	Bending	Bending	Bending	Bending
	1.132	+	-	-	Bending	Bending
	1.858	+	Bending/spandrel	Base/Pier	Bending	Base
	2.540	+	-	-	Bending	Base
	3.236	+	-	-	Bending	Pier
	4.036	+	Bending/spandrel	Pier/Base	Bending	Pier
(Parisi, Augenti and Prota, 2014)	0.373	+	Bending	Spandrel	Bending	Spandrel
(Vanin and Foraboschi, 2012)	0.300	+	Bending	Spandrel/base	Bending	Base
	0.179	+	Bending	Spandrel/base	Bending	Base
	0.090	+	Bending	Spandrel/bending	Bending	Bending
(Foraboschi, 2009)	0.270	+	-	-	Bending	Bending
	0.179	+	-	-	Bending	Bending
	0.090	+	-	-	Bending	Bending
(Korswagen *et al.*, 2017)	0.120	+	Bending	Bending/base	Bending	Bending
(Esposito and Ravenshorst, 2017)	0.340	+	Bending	Base	Bending	Spandrel
	0.340	-	Bending	Base	Bending	Spandrel
(Raijmaker and Vermeltfoort, 1992)	0.300	+	Spandrel	Base	Spandrel	Base

Table 4 Sensitivity study: effect of masonry bonding pattern and boundary conditions on force capacity.

Parameter	Variation	$\hat{H}_{mod}$
Masonry Bond	Stack	0.964
	English	1.000
	Flemish	1.232
	Running	1.240
Boundary conditions	Cantilever with “weak” spandrel	0.846
	Cantilever with “strong” spandrel	1.000
	Double-clamped	1.143
	Vertically restrained	1.455

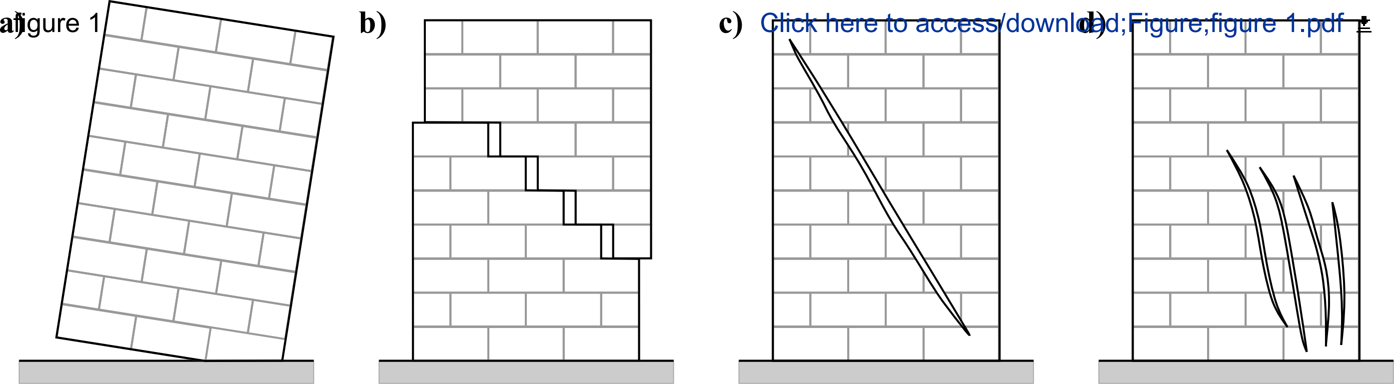
a)
b)
c)
d)

figure 2

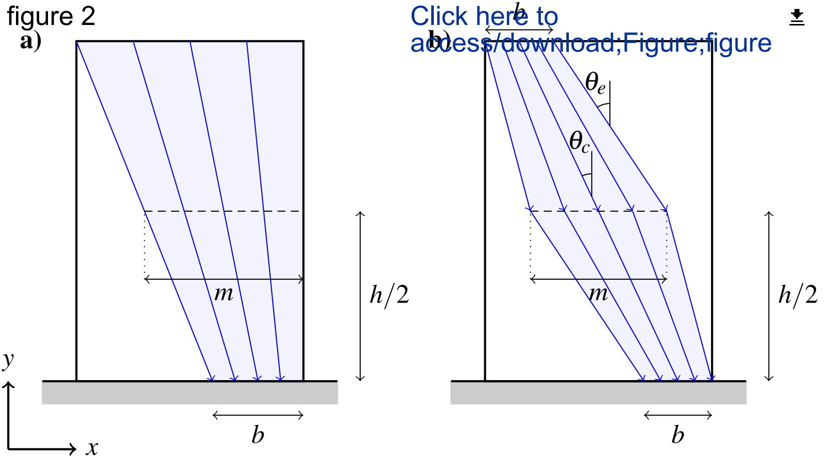

figure 3

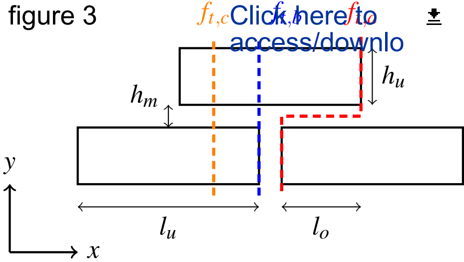

figure 4

Click here to access/download;Fi

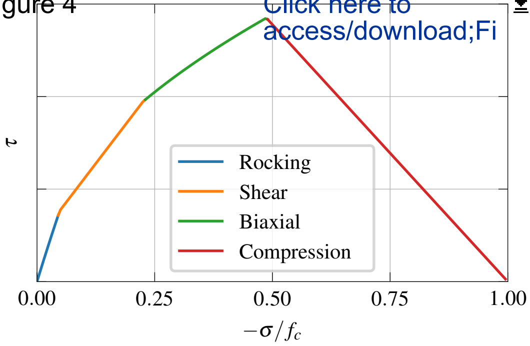

figure 5

Click here to access/download;Figure;figure 5.pdf

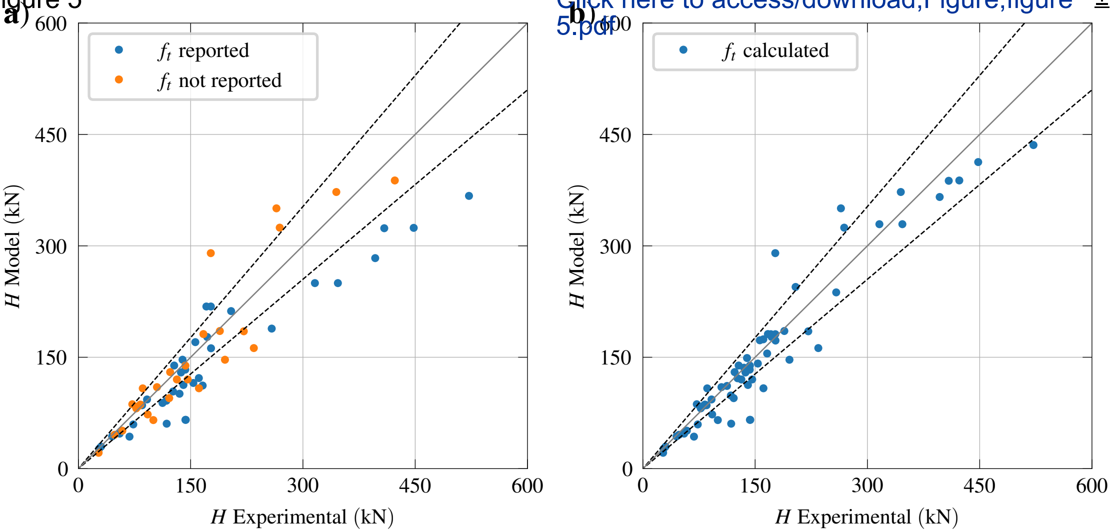

figure 6

Click here to access/download;Fi

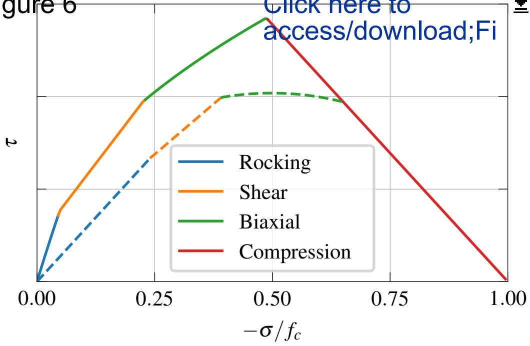

figure 7

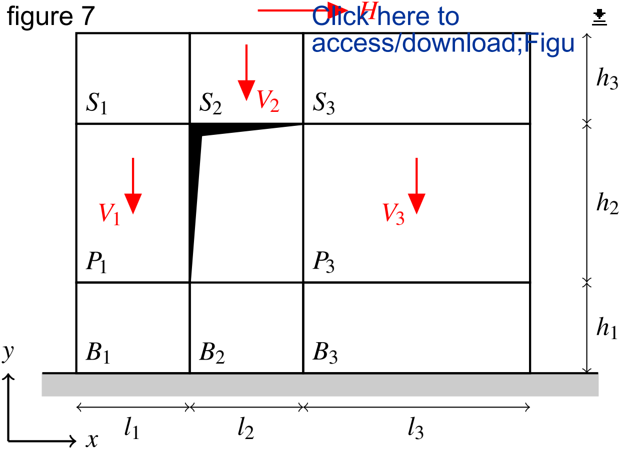

figure 8

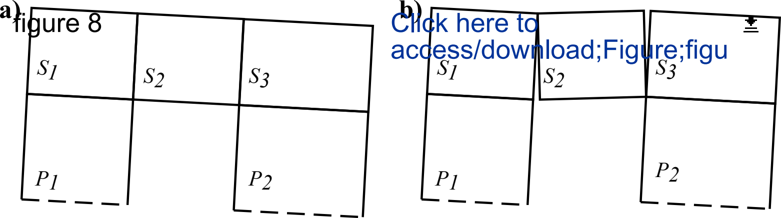

figure 9

Click here to access/download;Figure;figure

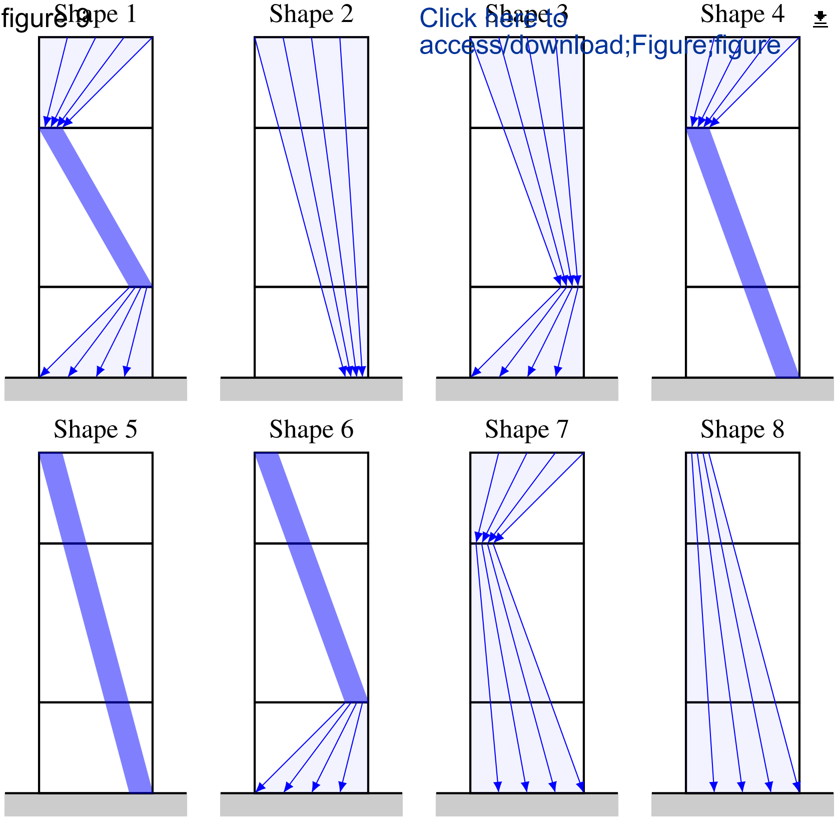

figure 10

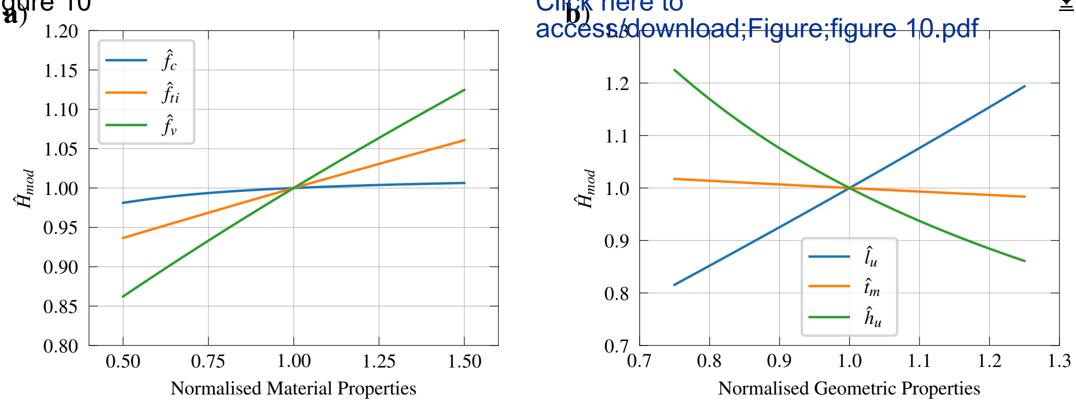
a)
1.20
1.15
1.10
1.05
1.00
0.95
0.90
0.85
0.80
$\hat{H}_{mod}$
$\hat{f}_c$
$\hat{f}_{ti}$
$\hat{f}_v$
0.50
0.75
1.00
1.25
1.50
Normalised Material Properties
b)
1.3
1.2
1.1
1.0
0.9
0.8
0.7
$\hat{H}_{mod}$
$\hat{l}_u$
$\hat{t}_m$
$\hat{h}_u$
0.7
0.8
0.9
1.0
1.1
1.2
1.3
Normalised Geometric Properties